

MECHANISMS IN THE SYNTHESIS OF FORSTERITE NANOPARTICLES BASED ON THERMODYNAMIC APPROACH

Alexandra AVRAM^a, Diana FLOREA^a, Firuta GOGA^a,
Maria GOREA^a, Aurora MOCANU^a, Gheorghe TOMOAI^{b,c},
Ioan PETEAN^a, Attila-Zsolt KUN^d, Ossi HOROVITZ^a,
Maria TOMOAI^{a,c,*}

ABSTRACT. Due to the ions in its structure, that have a variety of important roles in bone metabolism, forsterite (FS, Mg_2SiO_4) is a promising candidate for orthopedic and dental applications. This paper studies forsterite synthesized through two methods, namely sol-gel (FSsg) and precipitation (FSpp), based on a thermodynamic approach. Therefore, the precursor gel and precipitate were analyzed through thermal gravimetric (TG), differential thermal gravimetric (DTG) and differential scanning calorimetric (DSC) analysis. The FSsg and FSpp powders were characterized by X-ray powder diffraction (XRD) and atomic force microscopy (AFM). XRD reveals that the synthesized forsterite is of high crystallinity. As is evidenced by AFM, the average size of the nanoparticles is around 40 nm for FSsg and 30 nm for FSpp. The potential reaction mechanisms for the two synthesis routes were also established.

Keywords: *forsterite, sol-gel, precipitation method, synthesis mechanisms, thermodynamic approach*

-
- ^a Babes-Bolyai University of Cluj-Napoca, Research Center in Physical Chemistry, Faculty of Chemistry and Chemical Engineering, 11 Arany J. Str., RO-400028, Cluj-Napoca, Romania
^b Iuliu Hatieganu University of Medicine and Pharmacy, Orthopedics and Traumatology Department, 47 Traian Mosoiu Str., RO-400132 Cluj-Napoca, Romania
^c Academy of Romanian Scientists, 3 Ilfov Str., RO-050044, Bucharest, Romania
^d Department of Chemistry and Chemical Engineering, Hungarian Line of Study, Faculty of Chemistry and Chemical Engineering, Babeş-Bolyai University, Cluj-Napoca, Romania
* Corresponding author: mcotisel@gmail.com, maria.tomoaia@ubbcluj.ro



INTRODUCTION

Through various factors such as an inability to produce the optimal amount of bone material, an excessive resorption and an inadequate response during the bone remodelling process, the skeleton can acquire a fragility leading to various pathologies such as osteoporosis. Considering that the inorganic part of the bone includes hydroxyapatite and various phosphates, their highly biocompatible synthetic variants are very often used for orthopaedic applications, with a special emphasis on synthetic hydroxyapatite [1-17]. However, an orthopaedic implant also needs to withstand the pressures and heavy wear of regular use. Forsterite is a suitable candidate as an implant for load bearing applications due to its superior mechanical properties [18-23]. Its high biocompatibility and bioactivity – related to Mg^{2+} and SiO_4^{4-} ions in its composition, ions that are involved in various processes regarding bone formation [24-30] – would ensure an advantageous host-implant connection. There are a variety of studies concerning the ability of FS to produce HAP once immersed in SBF [31-35], its interaction with cells [36-39] as well as some, though few in vivo studies [33, 40].

Forsterite has been synthesized through various methods, such as solid-state synthesis [41, 42], sol-gel [43, 44], precipitation [45, 46], spray-drying [47] or mechanical activation [48, 49]. Opting for the right method is critical in the synthesis of materials as it can limit the precursors that can be used, impose certain temperature requirements for thermal treatments which can have an effect on particle dimensions, surface properties and the overall microarchitecture of the final product. For instance, an intrinsic antibacterial property has been reported for forsterite though the intensity of the effect may vary with the employed synthesis method. While a bactericidal effect was reported for precipitation-derived forsterite (10 mg/mL) a lack of activity was registered for sol-gel-derived one in the case of *S. aureus* [50]. Various degrees of inhibition (depending on FS concentration and pathogen) were also observed for both *Gram positive and Gram negative* strains for FS synthesized through a combustion method with glycine and urea [51]. Conversely, FS synthesized through mechanical activation was unable to have any effect at much larger concentrations (25-200 mg/mL) [52]. This discrepancy in results for the same material infers that differences among synthesis conditions could alter the final application. Therefore, a better understanding of synthesis mechanisms is needed to properly tailor a material for a specific application.

Accordingly, this work investigates the effects of synthesis conditions on obtained forsterite nanopowder. The purpose of this study is to synthesize FS by two different methods, namely sol-gel and precipitation and characterize the forsterite nanopowders in terms of phase purity, and powder morphology.

While both sol-gel and precipitation methods are widely used, to the best of our knowledge, current literature does not discuss the formation mechanism for forsterite synthesized specifically through these two methods. Therefore, considering the importance of having a deep understanding of the course of reaction we propose reaction pathways for both methods. For this purpose, as to keep the comparison of the two methods accurate, both samples (FSsg and FSpp) were synthesized using the same reagents and submitted to appropriate thermal treatment conditions.

The effects of the synthesis conditions on the physico-chemical properties were evaluated by X-ray powder diffraction (XRD) and atomic force microscopy (AFM).

RESULTS AND DISCUSSION

The choice of synthesis route is quite important as it can affect the characteristics of the final FS powder, namely the shape and size of nanoparticles, NPs, distribution and tendency of NPs agglomeration which in turn affect the structural homogeneity thus limiting FS potential applications. Different preparation methods of forsterite powder for medical applications are investigated in this work on the thermodynamic approach and it is found that the sol-gel and co-precipitation are appropriate procedures for this purpose. These fabrication methods are selected as they offer a better control of the process and the properties of the final product.

The sol-gel type of synthesis is very versatile due to the many parameters involved (type of precursors, type of solvents, pH, temperature), leading to a large array of nanostructured materials. However, in the case of multi-cation materials, there has to be a good control over the hydrolysis and condensation so as to avoid segregation. Co-precipitation on the other hand has the advantage of readily leading to homogenous materials with particles that are small in size by controlling nucleation through pH and temperature. However, the problem comes with ensuring the suitable conditions to secure the simultaneous precipitation of all species in the solution.

Thermal behaviour of forsterite precursor mixtures

Thermal analysis was performed on dried mixtures to define the minimum temperature needed for the nucleation of a forsterite phase. Figures 1 and 2 show the DSC curves (upper panels) and TG-DTG curves (lower panels) for the dried gel and dried precipitate respectively.

The thermal curves in Figure 1 show the processes that occur during the heating of the dried gel obtained after hydrolysis and condensation of precursors, followed by further drying. The removal of water remnants in the dried gel is characterized by an endothermic process up to around 230°C accompanied with a mass loss of around 22%. The following two exothermic processes, one between 233°C and 381°C and the second between 381°C and 465°C relate to the oxidation of organic components.

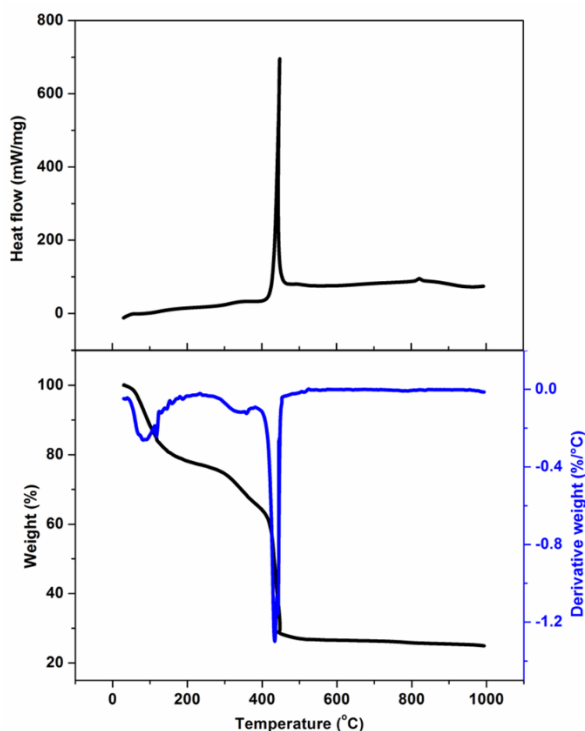
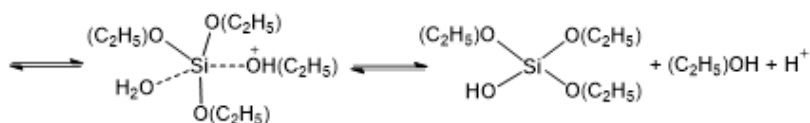
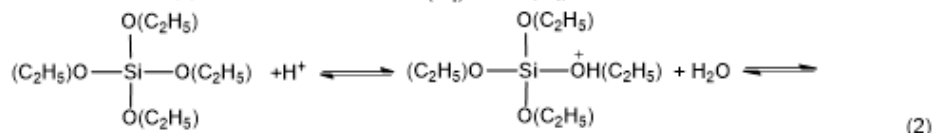
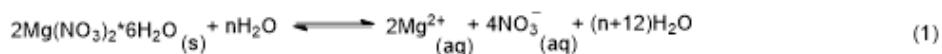


Figure 1. DSC (up) and TG/DTG (down) curves for FSsg dried gel (exo ↑, endo↓)

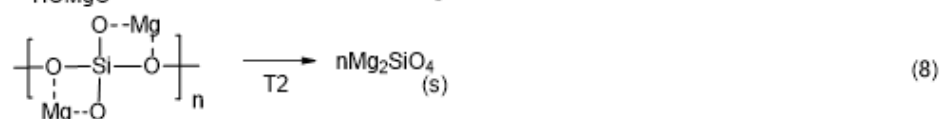
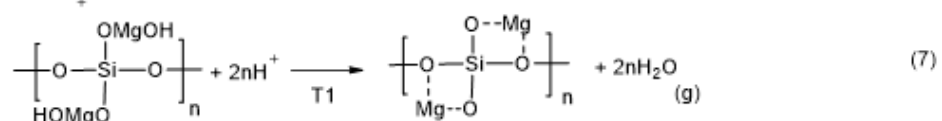
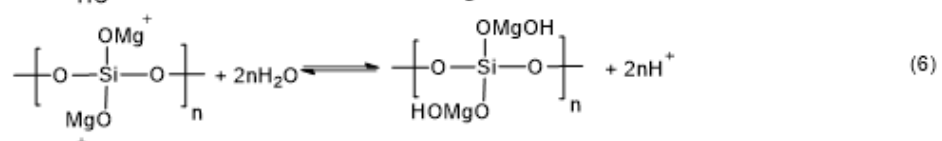
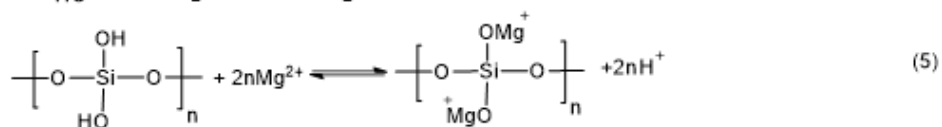
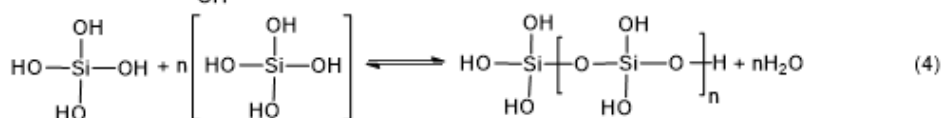
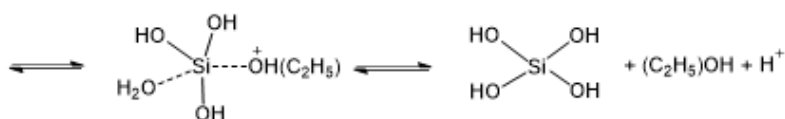
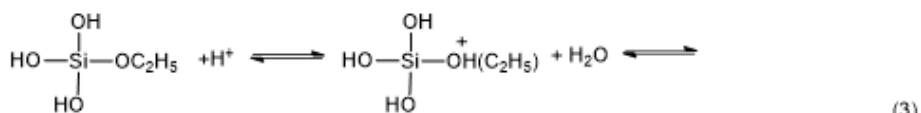
The volatile compounds formed lead to a mass loss of around 11.2% for the first exothermic process and 38.2% for the second one. Between around 500°C and 1000°C a slow mass loss of around 3% can be observed on the TG curve. This can be attributed to some remnants of organic volatile components. The smaller exothermic process without any significant mass loss that is observed at around 830°C can be assigned to the crystallization of Mg_2SiO_4 .

The potential mechanism in the sol-gel synthesis of forsterite is given in Scheme 1:

MECHANISMS IN THE SYNTHESIS OF FORSTERITE NANOPARTICLES
BASED ON THERMODYNAMIC APPROACH



(...)



Scheme 1. The mechanism in the sol-gel synthesis of forsterite, starting from precursors up to forsterite, FSsg, powder. Between Eq. (2) and Eq. (3), two similar steps of hydrolysis of the second and the third $-\text{OC}_2\text{H}_5$ group were not represented

When magnesium nitrate is dissolved in water, the Mg^{2+} and NO_3^- ions are set free (Eq. 1). Tetraethyl orthosilicate hydrolysis in acid catalysis (pH 1) proceeds in several stages, the four $-OC_2H_5$ groups being replaced in turn with $-OH$ groups, according to Eq. (2) for the first group and Eq. (3) for the last. The silicic acid thus formed undergoes a polycondensation process to a gel of poly(silicic acid) as shown in Eq. (4). Mg^{2+} ions substitute H^+ from OH groups of poly(silicic acid) as observed in Eq. 5 and bind HO^- ions from water (Eq. 6). In step (5) and step (6) the acidity of medium is progressively increased. At increased temperature (T_1), by elimination of HO^- in acid medium, Mg bridges are formed between oxygen atoms bonded to Si (Eq. 7), and finally, by dehydration the solid Mg_2SiO_4 powder results at higher temperature (T_2 , Eq. 8).

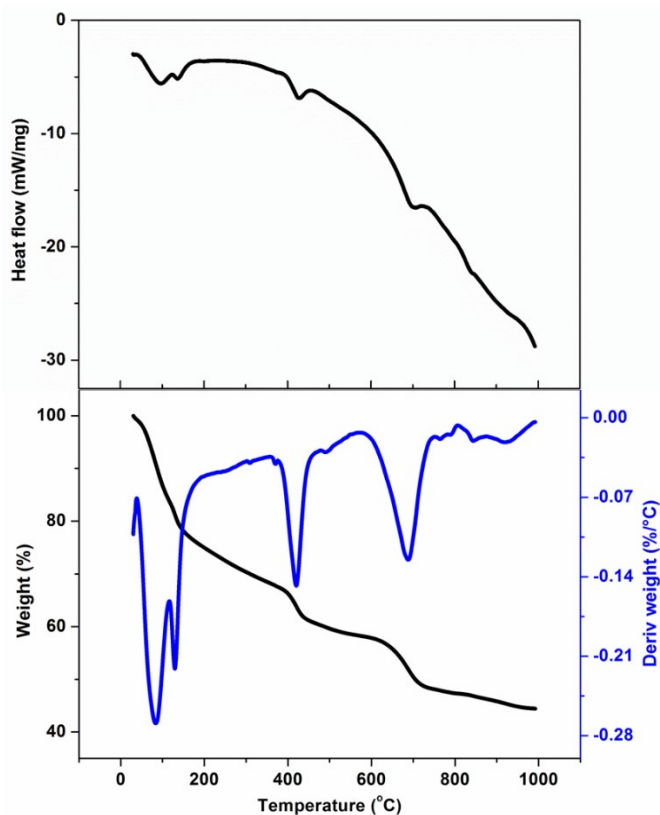


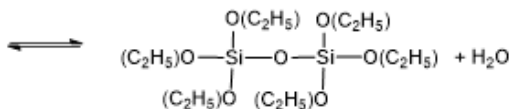
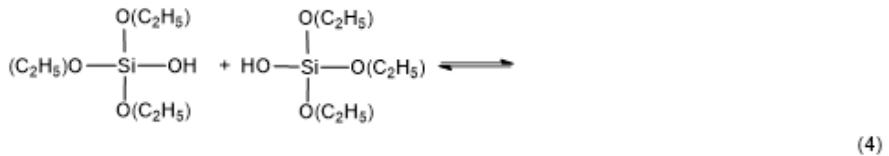
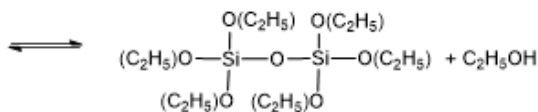
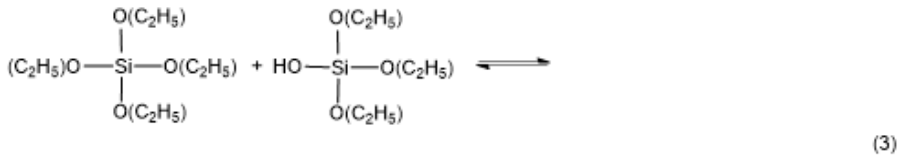
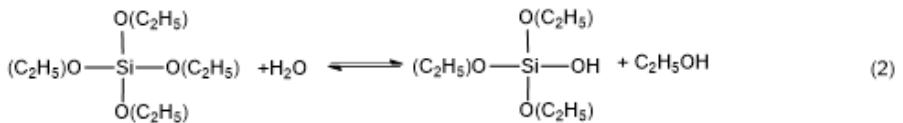
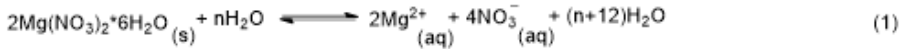
Figure 2. DSC (up) and TG/DTG (down) curves for FSpp dried precipitate (exo ↑, endo↓)

MECHANISMS IN THE SYNTHESIS OF FORSTERITE NANOPARTICLES
BASED ON THERMODYNAMIC APPROACH

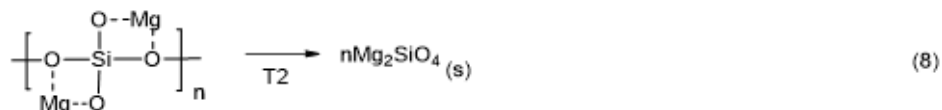
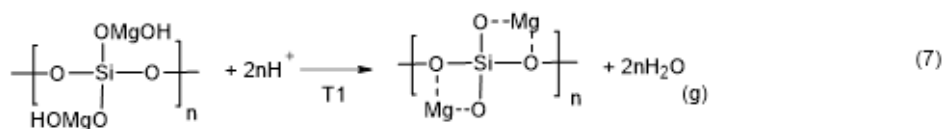
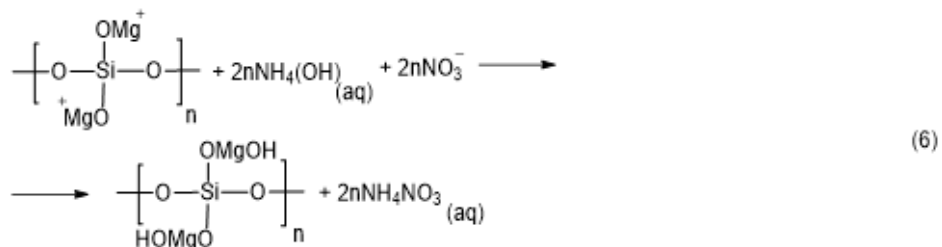
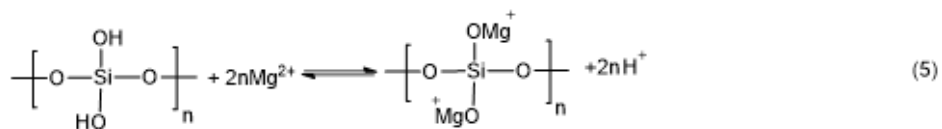
The thermal curves specific to the heating of the dried precipitate are presented in Figure 2. The removal of water remnants in the dried precipitate is characterized by two endothermic processes that occur up to 360°C. The mass loss attributed to these processes is of around 16% for the first and 16.2% for the second. Dehydroxylation of the -SiOH and -MgOH groups can be assigned to the next two endothermic processes, between 366°C and 582°C for -MgOH and at a higher temperature, up to 800°C for -SiOH.

The mass loss that accompanies these two endothermic effects is of around 10% for the first process and 13.6% for the second one. The overall mass loss for the sample is 55.8%.

A potential mechanism for the precipitation synthesis route is given in Scheme 2:



(...)



Scheme 2. The mechanism in the precipitation synthesis of forsterite, starting from precursors up to the formation of forsterite structure during thermal treatment

Eq. (1) is the same as in Scheme 1. The hydrolysis of TEOS proceeds in basic medium, the first step leading to triethyl orthosilicate Eq. (2). Condensation reactions may occur between tetraethyl orthosilicate molecules with ethanol elimination Eq. (3), or between tetraethyl orthosilicate and triethyl orthosilicate molecules with water elimination Eq. (4). The eventually resulted poly(silicic acid) binds Mg^{2+} ions as indicated in Eq. (5), which are subsequently hydroxylated in basic medium (NH_4OH), as shown in Eq. (6). By dehydroxylation at T1 as illustrated in Eq. (7) and through calcination at higher temperature T2 as given in Eq. (8), finally, the forsterite structure (Mg_2SiO_4 : FSpp) is formed.

Our results are a novelty on the mechanisms in FS synthesis, in both sol-gel and precipitation methods. The structure of intermediate products, during these syntheses, is shown in Scheme 1 and Scheme 2 and it is in accord with the findings obtained using Raman spectroscopy [45].

X-ray powder diffraction

Forsterite crystallizes in the orthorhombic system (space group Pbnm), having the following cell parameters: $a = 4.75 \text{ \AA}$, $b = 10.20 \text{ \AA}$ and $c = 5.98 \text{ \AA}$. The diffraction patterns for both forsterite materials, FSsg and FSpp, are presented in Figure 3. Clearly, the obtained powders have a well-defined crystallinity, more so in the case of FSsg.

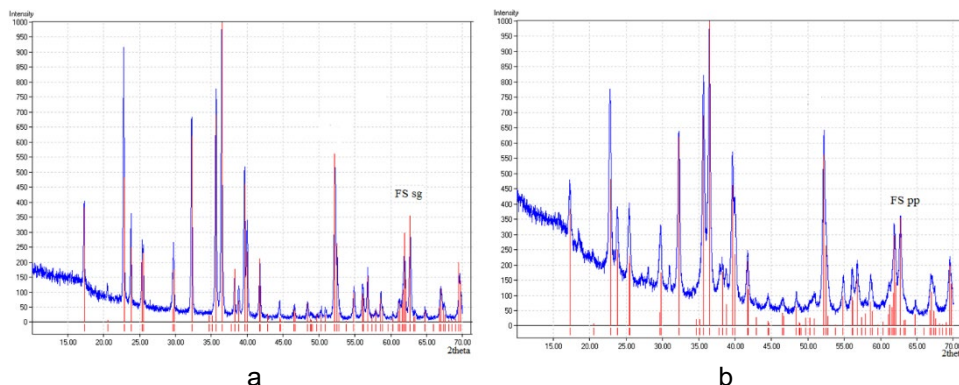


Figure 3. X-ray diffraction patterns for FSsg (a) and FSpp (b)

As it can be observed from the diffraction pattern in Figure 3a, forsterite is the only phase in the FSsg sample, indicating a complete reaction. On the other hand, in the case of FSpp, forsterite is present at around 98% (Figure 3b), the sample also containing traces of shistovite (around 1%, PDF 86-2333) and quartz (around 1%, PDF 83-0542). This can be explained by the higher reaction rate leading to an incomplete reaction for FSpp. A difference can also be observed in terms of crystallite sizes, around 54 nm for FSsg and 28 nm for FSpp. Again, this may be attributed to the fact that precipitation occurs more rapidly than the reactions involved in the sol-gel process. This result can also correlate with the particles size evidenced by AFM (Figure 4 for FSsg, and Figure 5 for FSpp) where the nanoparticles for FSpp are smaller (around 30 nm) than those for FSsg (around 40 nm).

Atomic force microscopy

The FSsg and FSpp nanoparticles exhibit the formation of a smooth adsorbed layer on glass as observed in Figures 4 and 5, particularly illustrated by low values of surface roughness (RMS). The nanoparticles are very well

individualized, even having a significant distance between them (Figures 4a and 5a). Their shape is rather spherical but, in some places, they tend to be slightly ovalized. The phase images given in Figure 4b for FSsg and in Figure 5b for FSpp show also the good individualization of both FSsg and FSpp nanoparticles, in total agreement with amplitude images (Figure 4c and Figure 5c) and 3D images (Figures 4d and 5d).

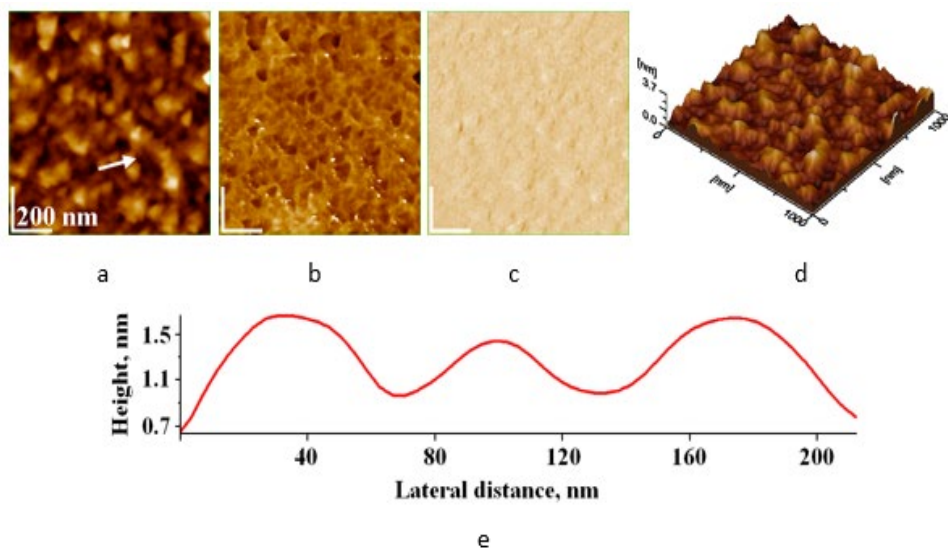


Figure 4. AFM images for FSsg nanoparticles adsorbed on glass: a) 2D topography image, b) phase image, c) amplitude image, d) 3D image, and e) cross section profile on the arrow in image (a). Scanning area: $1 \mu\text{m} \times 1 \mu\text{m}$. Particle size $43 \pm 6 \text{ nm}$; surface roughness (RMS, root mean square) $3 \pm 1 \text{ nm}$.

The profiles given in Figures 4e and 5e show the relatively rounded shape of the successively aligned nanoparticles of both FSsg and FSpp. The size of nanoparticles is bigger for FSsg (about 43 nm) than for FSpp (around 29 nm) in accord with the values found in XRD investigation. The standard deviation is determined on at least 3 independent scanned areas.

Further, in the case of sol-gel method, all material is kept in dispersion, first in the sol, then in the gel and dried gel. Thus, the transport of material is better, leading to a well-formed final FS structure without any other secondary phases (see Figure 3a). Also, this method leads to a better consolidation of the crystallites, so that the size of the particles is larger (as observed through AFM investigation, Figure 4).

MECHANISMS IN THE SYNTHESIS OF FORSTERITE NANOPARTICLES
BASED ON THERMODYNAMIC APPROACH

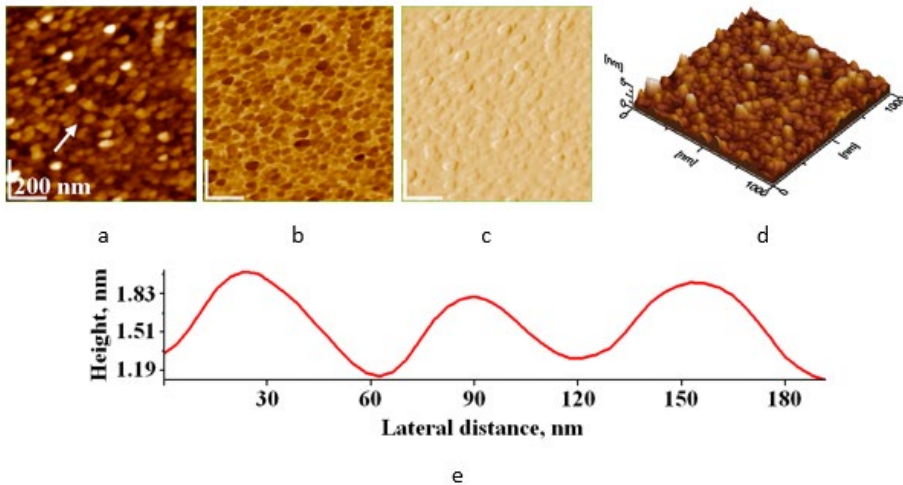


Figure 5. AFM imaging for FSpp nanoparticles adsorbed on glass: a) 2D topographic image, b) phase image, c) amplitude image, d) 3D image, and e) cross section profile on the arrow in image (a). Scanning area: $1 \mu\text{m} \times 1 \mu\text{m}$. Particle size: $29 \pm 4 \text{ nm}$; RMS about $4 \pm 2 \text{ nm}$.

Furthermore, in the FS synthesis by precipitation method, the precipitate obtained during the thermal treatment has a higher density, not being aerated as in the case of the sol-gel method. Thus, the transport of material is slower and as such traces of secondary phase might appear (see Figure 3b). Also, the forsterite particles are smaller, as observed through AFM approach (Figure 5).

CONCLUSIONS

The choice of synthesis route is quite important as it can affect the characteristics of the final powder – shape and size of nanoparticles, distribution and tendency of agglomeration which in turn affect the microstructural homogeneity of a ceramic and thus limit potential applications. The reaction mechanisms for both sol-gel and precipitation methods were proposed on the thermodynamic approach. Forsterite was successfully synthesized through both sol-gel (FSsg) and precipitation (FSpp) method, leading to smaller nanoparticles (30 nm) through precipitation method when compared to nanoparticles (40 nm) obtained by sol-gel method.

EXPERIMENTAL SECTION

Synthesis of forsterite

Forsterite nanopowder was synthesized through both a sol-gel (FSsg) and a precipitation (FSpp) method.

FSsg was synthesized following a molar ratio of Mg:Si=2:1 and using magnesium nitrate hexahydrate ($\text{Mg}(\text{NO}_3)_2 \cdot 6\text{H}_2\text{O}$, 99.5% purity, Merck) and tetraethyl orthosilicate ($\text{C}_8\text{H}_{20}\text{O}_4\text{Si}$ -TEOS, 99% assay, Merck) as precursors. An aqueous solution of magnesium nitrate was prepared to which TEOS was added, followed by a concentrated sucrose solution. After vigorous homogenization on a magnetic stirrer, nitric acid was added to the mixture until a pH=1 was achieved. Gel maturation was reached in normal conditions and the dried gel underwent a thermal treatment at 1000°C with a 2hour plateau at maximum temperature to ensure the formation of the forsterite phase.

FSpp was synthesized using the same molar ratio and precursors as for the sol-gel synthesis. A pH of 12 was reached adding ammonium hydroxide (Merck) to facilitate precipitation. The final precipitate was separated from the supernatant, washed with ultrapure water followed by a drying period. The dried precipitate was then thermally treated at 1000°C for 2h to form forsterite.

Analysis methods

Atomic force microscopy (AFM) was carried out on thin forsterite powder films deposited on glass substrates [53-58]. The analysis was performed using an AFM JEOL 4210 equipment operated in tapping mode with silicon nitride tip cantilevers (resonance frequency in the range 265-410 kHz and spring constant 20-75 N/m). Prior to AFM analysis, forsterite samples were ultrasounded with a Sonics Vibra-Cell, model VCX 750 (Sonics & Material Inc., Newtown, CT, USA equipment).

Thermal analysis (TG-DSC) of precursor gels was performed using a SDTQ600 TA Instruments thermal analyzer equipped with alumina crucibles. The analysis was carried out in air with a heating rate of 10°C / min for a temperature interval of 30-1000°C. [9, 50]

X-ray diffraction (XRD) spectra of the synthesized forsterite powders were acquired by using a Bruker D8 Advance diffractometer (Cu $\text{K}\alpha_1 = 1.5406 \text{ \AA}$, operated at 35 kV and 40 mA). The spectra were collected on a 20-80 2θ with a 0.02 $^\circ$ /sec step [59, 60].

All graphs were realized in OriginPro. All chemical equations were obtained using ChemDraw Professional.

ACKNOWLEDGMENTS

This work was supported by grants of the Ministry of Research, Innovation and Digitization, CNCS/CCCDI-UEFISCDI, project number 186 within PNCDI III.

REFERENCES

1. Gh. Tomoaia; M. Tomoaia-Cotisel; L. B. Pop; A. Pop; O. Horovitz; A. Mocanu; N. Jumate, L. D. Bobos; *Rev. Roum. Chim.*, **2011**, *56(10-11)*, 1039-1046.
2. C. Prejmerean; M. Tomoaia-Cotisel; E. Vasile; G. Furtos; L. B. Pop; M. Moldovan; C. Sarosi; I. Petean; *Int. J. Nano and Biomater.*, **2011**, *3(4)*, 344-359.
3. G. Furtos; M. Tomoaia-Cotisel; C. Garbo; M. Senila; N. Jumate; I. Vida-Simiti; C. Prejmerean; *Particul. Sci. Technol.*, **2013**, *31(4)*, 392-398.
4. Gh. Tomoaia; O. Soritau; M. Tomoaia-Cotisel; L.B. Pop; A. Pop; A. Mocanu; O. Horovitz, L. D. Bobos; *Powder. Technol.*, **2013**, *238*, 99-107.
5. A. Mocanu; G. Furtos; S. Rapuntean; O. Horovitz; C. Flore; C. Garbo; A. Danisteanu; Gh. Rapuntean; C. Prejmerean; M. Tomoaia-Cotisel; *Appl. Surf. Sci.*, **2014**, *298*, 225-235.
6. Gh. Tomoaia; A. Mocanu; I. Vida-Simiti; N. Jumate; L. D. Bobos; O. Soritau; M. Tomoaia-Cotisel; *Mater. Sci. Eng. C*, **2014**, *37*, 37-47.
7. P.T. Frangopol; A. Mocanu; V. Almasan; C. Garbo; R. Balint; G. Borodi; I. Bratu; O. Horovitz; M. Tomoaia-Cotisel; *Rev. Roum. Chim.*, **2016**, *61(4-5)*, 337-344.
8. A. Danisteanu; M. Gorea; A. Avram; S. Rapuntean; Gh. Tomoaia; A. Mocanu; C. Garbo; O. Horovitz; M. Tomoaia-Cotisel; *Stud. UBB Chem.*, **2016**, *61(3)*, 275-283.
9. E. Forizs; F. Goga; A. Avram; A. Mocanu; I. Petean; O. Horovitz; M. Tomoaia-Cotisel; *Stud. UBB Chem.*, **2017**, *62(4)*, 173-180.
10. A. Avram; T. Frentiu; O. Horovitz; A. Mocanu; F. Goga; M. Tomoaia-Cotisel; *Stud. UBB Chem.*, **2017**, *62(4)*, 93-104.
11. A. Mocanu; R. Balint; C. Garbo; L. Timis; I. Petean; O. Horovitz; M. Tomoaia-Cotisel; *Stud. UBB Chem.*, **2017**, *62(2)*, 95-103.
12. A. Avram; M. Gorea; R. Balint; L. Timis; S. Jitaru; A. Mocanu; M. Tomoaia-Cotisel; *Stud. UBB Chem.*, **2017**, *62(4)*, 81-92.
13. S. Rapuntean; P. T. Frangopol; I. Hodisan; Gh. Tomoaia; D. Oltean-Dan; A. Mocanu; C. Prejmerean; O. Soritau; L. Z. Racz; M. Tomoaia-Cotisel; *Rev. Chim. (Bucharest)*, **2018**, *69(12)*, 3537-3444.
14. D. Oltean-Dan; G. B. Dogaru; M. Tomoaia-Cotisel; D. Apostu; A. Mester; H. R. C. Benea; M. G. Paiusan; E. M. Jianu; A. Mocanu; R. Balint; C. O. Popa; C. Berce; G. I. Bodizs; A. M. Toader; Gh. Tomoaia; *Int. J. Nanomed.*, **2019**, *14*, 5799-5816.

15. D. Oltean-Dan; G.-B. Dogaru; E.-M. Jianu; S. Riga; M. Tomoiaia-Cotisel; A. Mocanu; L. Barbu-Tudoran; Gh. Tomoiaia; *Micromachines*, **2021**, *12*(11), 1325.
16. A. Mocanu; P.T. Frangopol; R. Balint; O. Cadar; I.M. Vancea; R. Mantiu; O. Horovitz, M. Tomoiaia-Cotisel; *Stud. UBB Chem.*, **2021**, *66*(3), 195-207.
17. A. Mocanu; O. Cadar; P.T. Frangopol; I. Petean; Gh. Tomoiaia; G.-A. Paltinean; C.P. Racz; O. Horovitz; M. Tomoiaia-Cotisel; *R. Soc. Open. Sci.*, **2021**, *8*(1), 201785.
18. S. Ramesh; A. Yaghoubi; K.Y.S. Lee; K.M.C. Chin; J. Purbolaksono; M. Hamdi; M.A. Hassan; *J. Mech. Behav. Biomed. Mater.*, **2013**, *25*, 63-69.
19. F.S. Sayyedani; M.H. Fathi; H. Edris; A. Doostmohammadi; V. Mortazavi; A. Hanifi; *Ceram. Int.*, **2014**, *40*, 10743-10748.
20. S. Pratapa; W.D. Handoko; U. Nurbaiti; M. Mashuri; *Ceram. Int.*, **2017**, *43*, 7172-7176.
21. S.A. Hassanzadeh-Tabrizi; *Ceram. Int.*, **2017**, *43*, 15714- 15718.
22. M. Gorea; M.-A. Naghiu; A. Avram; I. Petean; M. Tomoiaia-Cotisel; *Stud. UBB Chem.*, **2019**, *64*(2(2)), 383-392.
23. G. Furtos; M. A. Naghiu; H. Declercq; M. Gorea; C. Prejmerean; O. Pana; M. Tomoiaia-Cotisel; *J. Biomed. Mater. Res. Part B*, **2016**, *104*(7), 1290-1301.
24. F.I. Wolfe; A. Cittadini; *Mol. Aspects Med.*, **2003**, *24*, 3-9.
25. R.K. Rude; H.E. Gruber; *J. Nutr. Biochem.*, **2004**, *15*, 710-716.
26. S. Castiglioni; A. Cazzaniga; W. Albisetti; J.A.M. Maier; *Nutrients*, **2013**, *5*, 3022-3033.
27. L.Y. He; X.M. Zhang; B. Liu; Y. Tian; W.H. Ma; *Braz. J. Med. Biol. Res.*, **2016**, *49*(7), e5257.
28. P. Han; C. Wu; Y. Xiao; *Biomater. Sci.*, **2013**, *1*, 379-392.
29. K. Dashnyam; A. El-Fiqi; J.O. Buitrago; R.A. Perez; J.C. Knowles; H.-W. Kim; *J. Tissue Eng.*, **2017**, *8*, 2041731417707339.
30. W. Gotz; E. Tobiasch; S. Witzleben; M. Schulze; *Pharmaceutics*, **2019**, *11*(3), 117.
31. M. Gorea; M.-A. Naghiu; M. Tomoiaia-Cotisel; *Ceram.-Silk.*, **2013**, *57*(2), 87-91.
32. R. Gheitanchi; M. Kharaziha; R. Emadi; *Ceram. Int.*, **2017**, *43*, 12018-12025.
33. K.B. Devi; B. Tripathy; A. Roy; B. Lee; P.N. Kumta; S.K. Nandi; M. Roy; *ACS Biomater. Sci. Eng.*, **2019**, *5*, 530-543.
34. F. Tavangarian; R. Emadi; *Ceram. Int.*, **2011**, *37*, 2275-2280.
35. M.A. Naghiu; M. Gorea; E. Mutch; F. Kristaly; M. Tomoiaia-Cotisel; *J. Mater. Sci. Technol.*, **2013**, *29*(7), 628-632.
36. G. Krishnamurthy; S. Mohan; N.A. Yahya; A. Mansor; M.R. Murali; H.R.B. Raghavendran; R. Choudhary; S. Sasikumar; T. Kamarul; *PLoS ONE*, **2019**, *14*(3), e0214212.
37. M. Kharaziha; M.H. Fathi; *J. Mech. Behav. Biomed. Mater.*, **2010**, *3*, 530-537.
38. S. Ni; L. Chou; J. Chang; *Ceram. Int.*, **2007**, *33*, 83-88.
39. M. Kheradmandfard; S.F. Kashani-Bozorg; A.H. Noori-Alfesharaki; A.Z. Kharazi; M. Kheradmandfard; N. Abutalebi; *Mat. Sci. Eng. C*, **2018**, *92*, 236-244.
40. K.B. Devi; B. Tripathy; P.N. Kumta; S.K. Nandi; M. Roy; *ACS Biomater. Sci. Eng.*, **2018**, *5*, 2126-2133.

41. L. Chen; G. Ye; Q. Wang; B. Blanpain; A. Malfiet; M. Guo; *Ceram. Int.*, **2015**, 41(2(A)), 2234–2239
42. L. Mathur; S.K.S. Hossain; M.R. Majhi; P.K. Roy; *Bol. Soc. Esp. Ceram. Vidr.*, **2018**, 57(3), 112–118.
43. F. Ghariani; R. Fezei; A.H. Hamzaoui; *J. Sol-Gel Sci. Technol.*, **2018**, 88, 100-104.
44. A.M. Nojehdeh; F. Moghaddam; M.T. Hamedani; *J Sol-Gel Sci Technol.*, **2022**, 107(1), 1-9.
45. R.Y.S. Zampiva; L.H. Acauan; L. Moreira dos Santos; R.H. Ribeiro de Castro; A. Kopp Alves; C. Perez Bergman; *Ceram. Int.*, **2017**, 43(18), 16225-16231.
46. A. Avram; M. Gorea; S. Rapuntean; A. Mocanu; G.A. Paltinean; C. Varhelyi Jr.; O. Horovitz; M. Tomoaia-Cotisel; *Rev. Chim. (Bucharest)*, **2020**, 71(1), 13-21.
47. A. Douy; *J. Sol-Gel Sci. Technol.*, **2002**, 24, 221-228.
48. R. Saidi; M. Fathi; H. Salimijazi; M. Mohammadrezaie; *J. Sol-Gel Sci. Technol.*, **2017**, 81(3), 734-740.
49. U. Nurbaiti; Darminto; Triwikantoro; M. Zainuri; S. Pratapa; *Ceram. Int.*, **2018**, 44, 5543–5549.
50. A. Avram; S. Rapuntean; M. Gorea; Gh. Tomoaia; A. Mocanu; O. Horovitz; Gh. Rapuntean; M. Tomoaia-Cotisel; *Environ. Sci. Pollut. Res.*, **2022**, 29, 77097–77112.
51. R. Choudhary; A. Chatterjee; S.K. Venkatraman; S. Koppala; J. Abraham; S. Swamiappan; *Bioact. Mater.*, **2018**, 3, 218-224.
52. M. Saqaei; M. Fathi; H. Edris; V. Mortazavi; N. Hosseini; *Adv. Powder Technol.*, **2016**, 27, 1922-1932.
53. M. Tomoaia-Cotisel; A. Tomoaia-Cotisel; T. Yupsanis; Gh. Tomoaia; I. Balea; A. Mocanu; Cs. Racz; *Rev. Roum. Chim.*, **2006**, 51(12), 1181-1185.
54. O. Horovitz; Gh. Tomoaia; A. Mocanu; T. Yupsanis; M. Tomoaia-Cotisel; *Gold Bull.*, **2007**, 40(4), 295-304.
55. U. V. Zdrenghea; Gh. Tomoaia; D.-V. Pop-Toader; A. Mocanu; O. Horovitz; M. Tomoaia-Cotisel; *Comb. Chem. High Throughput Screen.*, **2011**, 14(4), 237-247.
56. L.Z. Racz; G.-A. Paltinean; I. Petean; Gh. Tomoaia; L.C. Pop; G. Arghir; E. Levei; A. Mocanu; C.-P. Racz; M. Tomoaia-Cotisel; *Studia UBB Chem.*, **2022**, 67(3), 61-74.
57. A. Mocanu; R.D. Pasca; Gh. Tomoaia; C. Garbo; P.T. Frangopol; O. Horovitz; M. Tomoaia-Cotisel; *Int. J. Nanomed*, **2013**, 8, 3867-3874.
58. C.-P. Racz; L.Z. Racz; C.G. Floare; Gh. Tomoaia; O. Horovitz; S. Riga; I. Kacso; Gh. Borodi; M. Sarkozi; A. Mocanu; C. Roman; M. Tomoaia-Cotisel; *Food Hydrocoll.*, **2023**, 139, 1088547.
59. Cs.-P. Racz; S. Santa; M. Tomoaia-Cotisel; Gh. Borodi; I. Kacso; A. Pirnau; I. Bratu; *J. Incl. Phenom. Macrocycl. Chem.*, **2013**, 76, 193–199.
60. C. Garbo; J. Locs; M. D'Este; G. Demazeau; A. Mocanu; C. Roman; O. Horovitz; M. Tomoaia-Cotisel; *Int. J. Nanomed.*, **2020**, 15, 1037-1058.

